OPTICA

Nonlocal metasurface for circularly polarized light detection

Jiho Hong,[1] Jorik van de Groep,[1,2] Nayeun Lee,[1] Soo Jin Kim,[1,3] Philippe Lalanne,[4] Pieter G. Kik,[1,5] and Mark L. Brongersma[1,*]

[1]Geballe Laboratory for Advanced Materials, Stanford University, Stanford, California 94305, USA
[2]Current address: Van der Waals–Zeeman Institute for Experimental Physics, Institute of Physics, University of Amsterdam, 1098 XH Amsterdam, The Netherlands
[3]Current address: School of Electrical Engineering, Korea University, Seoul 02841, Republic of Korea
[4]Laboratoire Photonique, Numérique et Nanosciences (LP2N), Institut d'Optique Graduate School, University of Bordeaux, CNRS, 33400 Talence Cedex, France
[5]CREOL, The College of Optics and Photonics, University of Central Florida, Orlando, Florida 32816, USA
*Corresponding author: brongersma@stanford.edu

Received 21 June 2022; revised 9 November 2022; accepted 11 November 2022; published 20 January 2023

Modern-day sensing and imaging applications increasingly rely on accurate measurements of the primary physical quantities associated with light waves: intensity, wavelength, directionality, and polarization. These are conventionally performed with a series of bulky optical elements, but recently, it has been recognized that optical resonances in nanostructures can be engineered to achieve selective photodetection of light waves with a specific set of predetermined properties. Here, we theoretically illustrate how a thin silicon layer can be patterned into a dislocated nanowire-array that affords detection of circularly polarized light with an efficiency that reaches the theoretical limit for circular dichroism of a planar detector in a symmetric external environment. The presence of a periodic arrangement of dislocations is essential in achieving such unparalleled performance as they enable selective excitation of nonlocal, guided-mode resonances for one handedness of light. We also experimentally demonstrate compact, high-performance chiral photodetectors created from these dislocated nanowire-arrays. This work highlights the critical role defects can play in enabling new nanophotonic functions and devices.

https://doi.org/10.1364/OPTICA.468252

1. INTRODUCTION

Light exhibits distinct interactions with materials that can depend on the intensity, wavelength, incident direction, and polarization state. In nanostructures, we can harness plasmonic and Mie resonances to further tailor the ways in which light interacts with matter. Whereas such resonant structures have primarily been exploited to control the flow of light, they can also be employed to uncover the nature of the light that is incident from an optical scene. Dense, planar arrays of nanostructures, termed metasurfaces, have been particularly useful for this purpose as their diffraction behavior is very sensitively dependent on the properties of light waves. For example, they have successfully been used to perform spectropolarimetry by decomposing plane waves into a set of separated beams that each carry information on the incident angle, spectral content, and polarization state [1–8]. However, such metasurfaces need to be used in conjunction with a separate image sensor to create a complete spectro-polarimetric system. To allow further device integration, it is critical to explore whether the spectral/polarization decomposition and the photodetection processes can be combined in a single metasurface. Recently, semiconductor nanowire (NW) arrays have already been incorporated in multispectral detection and imaging systems [9,10]. To gain the maximum possible information from a data stream or optical scene, we need to also determine the state of polarization through a measurement of the Stokes parameters [11]. Using anisotropic semiconductor NWs [12] or metallic slits [13] in the photodetection, it is straightforward to distinguish linear states of polarization. However, the optical detection of circularly polarized light (CPL) is inherently more challenging. Such waves are comprised of two orthogonally polarized light waves for which the electric fields are oscillating with a $\pm\pi/2$ phase shift, and this relative phase information is lost in the photodetection process. As a result, CPL detection typically involves the use of a quarter-wave plate and linear polarizer on top of a (non-chiral) photodetector. In fact, many invertebrates such as mantis shrimp, cuttlefish, bees, and crickets have developed such compound elements to create CPL-sensitive detection systems for communication and visual contrast enhancement [14]. It is, however, well worth exploring new ways to measure the properties of CPL, given its increasingly prominent role in many applications, including quantum optics [15] and communication [16], drug design and development

[17], remote sensing [18] and spectropolarimetry [19], imaging [20], valley optoelectronics [21], and topological photonics [22]. Recent pioneering approaches include detectors that employ chiral organic molecules and semiconductors [23–25] and chiral plasmonic structures [26,27]. Plasmonic structures can show particularly high circular dichroism (CD), i.e., differential absorption for left- and right-handed CPL [27–30], but metals tend to make poor photodetectors that can only rely on inefficient hot electron emission. To boost the responsivity, it is highly desirable to explore whether chiral detectors can be made from high electrical-performance, inorganic, achiral semiconductors. Here, we show that a dislocated silicon nanowire (Si NW) metasurface can effectively detect and distinguish left- and right-handed CPL without the need of external filters or waveplates.

2. RESULTS

Figure 1(a) shows a conceptual schematic of our proposed CD photodetector. It features a dense array of custom-designed Si NWs on a transparent substrate. The unique shape of the NWs with a periodic array of kinks is engineered to facilitate excitation of a nonlocal guided-mode resonance by normally incident CPL with one selected handedness while transmitting light waves of the opposite handedness. Recently, there has been an increased interest in flat optical elements with nonlocal optical resonances [31–37] as they enable high-performance imaging, sensing, and modulation functions. These flat optical elements display more spatially extended, high optical, quality-factor modes and momentum-dependent transfer functions. In our case, the nonlocal resonance selectively enables substantial optical absorption and photocarrier generation in the semiconductor material for the circular polarization (CP) of interest. The polarization can therefore be determined through a measurement of the photocurrent upon application of a small bias voltage to the electrodes. A scanning electron micrograph (SEM) of an array fabricated by electron beam lithography is shown in Fig. 1(b).

Before we provide a detailed mechanistic picture of the metasurface operation, we evaluate the fundamental performance limit for this type of device using coupled-mode theory [38,39]. Because of its two-dimensional nature, the detector can be treated as a single-mode optical resonator in a symmetric external environment. The incident CPL can follow a direct transmission pathway and a resonant pathway through the nanopatterned semiconductor layer [Fig. 1(c)]. When the light follows the resonant pathway and the guided resonance is excited, it leads to significantly increased energy storage and light absorption. To maximize the CD, we would ideally construct a situation where the incident light can only excite the resonance when its polarization matches the desired handedness. In our example, this will be right-handed circular polarization (RCP). To achieve the strongest possible light absorption, a fraction of the in-coupled light needs to couple back out into free space in order to effectively cancel out the directly transmitted light through destructive interference. The reciprocal nature of this device enforces that on resonance, the out-coupled light from

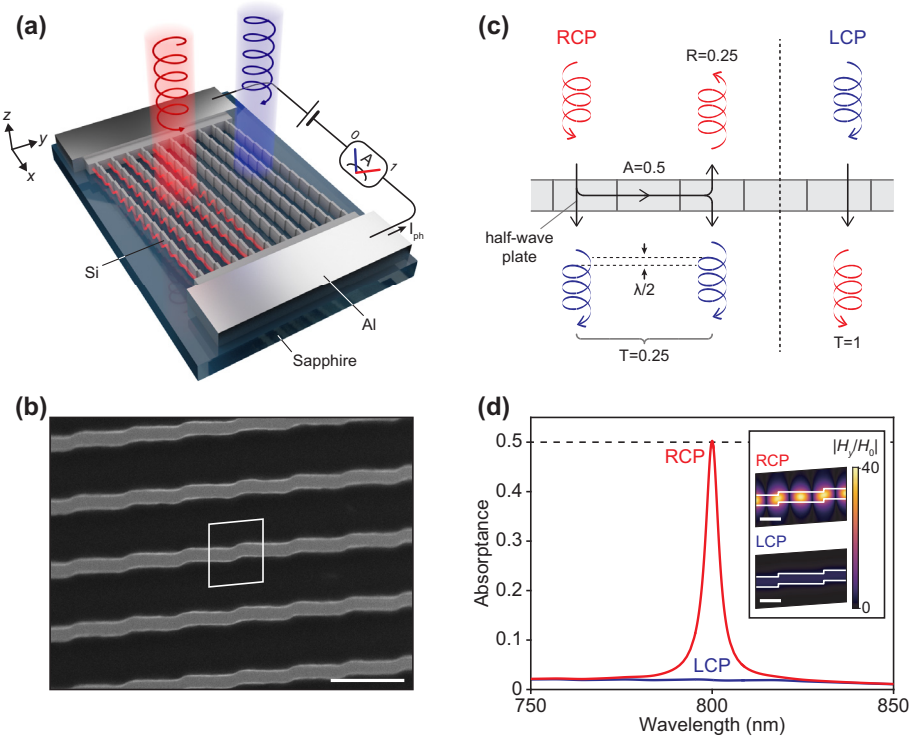

Fig. 1. Dislocated high-index semiconductor metasurfaces for CD. (a) The schematic of a CD photodetector using dislocated high-index semiconductor metasurfaces. A dislocated Si NW metasurface displays resonant absorption for a CP of interest (RCP, red) while transmitting the other (LCP, blue), allowing an electrical read-out of an incident CP. (b) The SEM of fabricated Si nanostructures. A unit cell of the periodic structures is outlined by the white box. Scale bar, 500 nm. (c) The illustration of an optically resonant nanopatterned semiconductor layer in free space interacting with incident RCP (left) and LCP (right) at critical coupling. (d) The simulated optical absorption spectra of a dislocated Si NW metasurface suspended in free space for RCP (red) and LCP (blue). The Si metasurface is designed to present resonant absorption for the RCP at $\lambda = 800$ nm. The theoretical limit of absorptance is indicated by the black dashed line. Inset: Normalized magnetic field distributions ($\lambda = 800$ nm) in the median plane of two adjacent unit cells for the RCP (top) and the LCP (bottom). Scale bar, 200 nm.

the resonator changes its handedness in the transmission direction (Supplement 1, Note 1). As a result, we see that left-handed circular polarization (LCP) emerges given an RCP incident beam. In order for the directly transmitted light to interfere destructively with the out-coupled light, its polarization should thus also have the opposite handedness and incur a π phase delay with respect to the resonant pathway. In other words, it is essential that the slab serves as a half-wave plate for the direct transmission channel. This is a key insight of our analysis as it provides valuable intuition about possible device designs. Analogous to optical absorption in an ultrathin and freely suspended metallic film [40], the theoretical limit for the absorptance of the RCP light is 0.5 at critical coupling when both the total transmittance and reflectance are 0.25.

Leveraging the insights derived from coupled-mode theory, we aim to identify a nanostructure design for the suspended silicon (Si) film that can both serve as a half-wave plate for the direct transmission pathway and only exhibit an optical resonance for the RCP light. Figure 1(d) shows the optical absorption behavior of our successfully optimized design, as obtained by finite-element simulations. As desired, the spectrum for LCP illumination shows a low and relatively constant absorptance across the wavelength range of interest. This results from the non-resonant absorption channel where light is directly transmitted through the film with little dissipation in the Si. On the other hand, the absorption spectrum for the RCP light displays a spectrally narrow resonance with a high optical quality factor, $Q = 180$. The metasurface achieves critical coupling, and the absorptance on resonance is just above the theoretically predicted limit. The slightly larger absorption results from the small amount of non-resonant absorption in the finite-thickness film. The magnetic field distributions in the nanostructured layer on and off resonance are shown as insets. For RCP, the high-Q resonance gives rise to a strong field enhancement inside the NWs. This enables significant optical absorption in the Si despite its weak material absorption. In the following, we will discuss the intuitive design for the NWs and the physics behind the operation of our CPL detector.

In the design of our metasurface-based photodetector, we aim to use high electrical-performance semiconductors and avoid the use of complex and hard-to-integrate three-dimensional chiral systems, such as arrays of helices [28] and twisted optical metamaterials [29,41,42]. Fortuitously, it has been shown that a strong CD can also be obtained in planar chiral metasurfaces [27,43,44], i.e., metasurfaces that are distinguishable from their mirror images (enantiomers) with respect to a line in the plane of the structure. We start the design of our planar chiral metasurface by considering the optical properties of a dense, subwavelength array of straight Si NWs. Such anisotropic, non-diffractive structures exhibit artificial birefringence and can be engineered to serve as a half-wave plate [45], satisfying our first design requirement. We can also easily turn NWs into photodetectors by electrically contacting both ends, and they have already been implemented to selectively detect light of specific wavelengths, linear polarizations, and incident angles [12,46]. Without modification, linear NW-arrays exhibit identical optical responses for both CPs. However, the introduction of a series of localized displacements in the NWs [see Fig. 1(a, b)] renders the metasurface planar chiral and produces distinct optical responses for the RCP and the LCP light. These displacements are reminiscent of the atomic displacements that occur near a dislocation core in a real crystal [47], and for this reason, we term the structure a dislocated NW metasurface. Whereas the architecture of a metamaterial crystal is typically linked to its optical properties, recent work has also demonstrated the powerful benefits of controllably introducing defects and disorder to achieve new properties not seen in perfect crystals [48–53]. In engineered metamaterials, the ability to continuously tune the geometry and size of defects can afford profound new insights into the evolution of certain physical properties with varying defect parameters. In turn, such fine-tuning allows one to reach fundamental performance limits. Here, we follow this approach for our dislocated NW metasurfaces.

We employ a scattered field formalism (Supplement 1, Note 2) to show how the introduction of dislocations can have a dramatic impact on the optical properties of the metasurface. Our analysis indicates that the dislocations can serve as secondary localized sources of scattered fields that control the coupling of free-space light waves to quasi-guided, nonlocal modes supported by the NW array. At the elementary level, this point is illustrated in Fig. 2(a) for a single, dislocated, 50-nm-thick Si NW illuminated by transverse-magnetic (TM) incident light, where the electric field is directed along the NW axis. The incident electric field drives an oscillating displacement current D (dark blue arrows) along the semi-infinite NW (x-direction). The introduction of a kink in the NW results in discontinuities in the permittivity and accumulation of positive and negative surface charges at the newly created corners (Supplement 1, Fig. S2). The surface charge distributions for this very thin NW form a localized electric dipole that is oriented perpendicular to the incident electric field. This dipole orientation allows effective radiation into the guided modes of both semi-infinite NWs.

Next, we aim to create dislocations capable of selectively coupling the CPL of one desired handedness. We show a conceptually intuitive strategy that builds on the observation that CPL is composed of two orthogonally polarized light waves for which the electric fields are oscillating with a $\pm\pi/2$ phase shift. If the dislocations can enable the coupling of both the incident TM and the orthogonal, i.e., transverse-electric (TE) polarizations to the same guided mode of the NW, then we can control the excitation efficiency of the guided-mode resonance by manipulating their optical interference. Constructive/destructive interference and a concomitant high/low excitation efficiency can result depending on the relative phase of the two excited waves. Dislocations in larger NW sizes can accomplish this as they can produce a variety of higher-order multipolar sources of scattered fields. Through the scattered field formalism, we can identify the nature of the multipolar sources as it naturally connects the oscillating charge distributions at the dislocations to the excited resonances in the NWs [54]. For example, the illumination of a dislocated 180-nm-thick NW with 800 nm light gives rise to the formation of an electric quadrupole for TM-polarization [Fig. 2(b)] and a magnetic dipole for TE polarization [Fig. 2(c)]. The electric quadrupole, induced for TM polarization, can be considered as a set of electric dipoles oriented anti-parallel in the horizontal and vertical directions [as illustrated in Fig. 2(b)]. As they are placed off the NW axes on both sides, these anti-parallel pairs can radiate into the semi-infinite NWs with the same parity as a magnetic dipole. For TE polarization, similarly to the electric dipole induced in a thin Si NW [Fig. 2(a)], the magnetic dipole is oriented perpendicular to the incident magnetic field. This polarization conversion is a key ingredient for our strategy as it allows effective coupling into the same guided mode for the two orthogonal polarizations of the

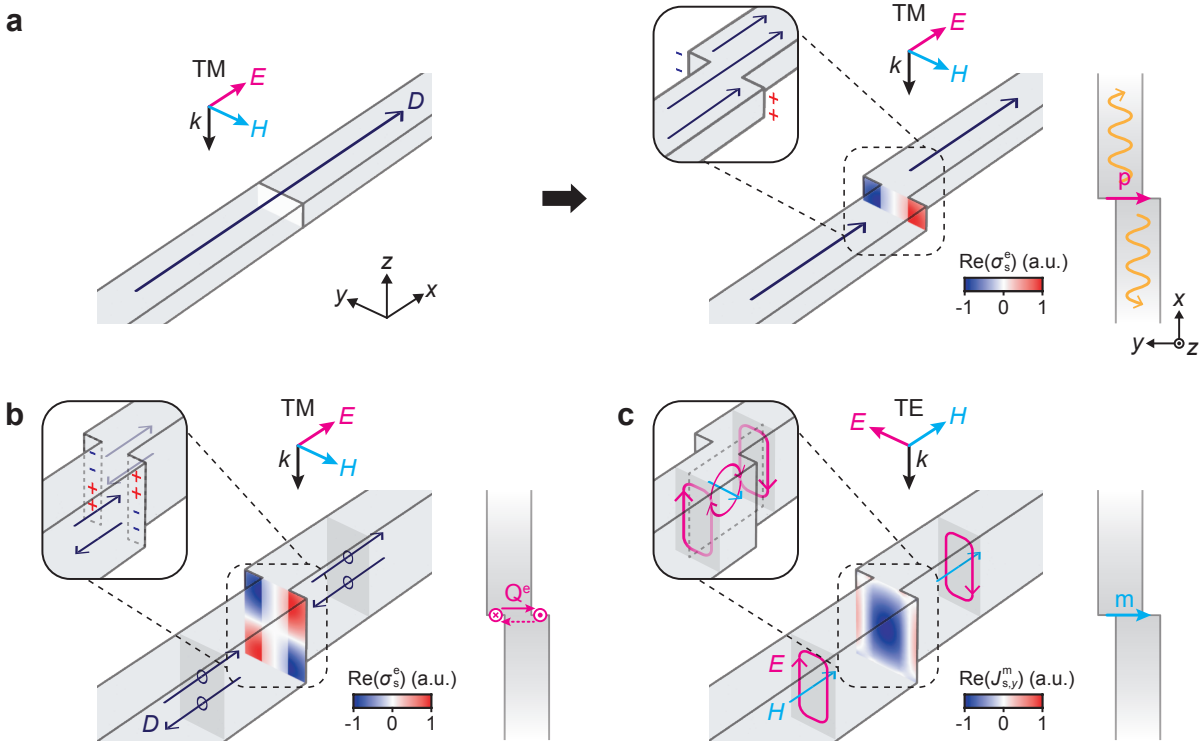

Fig. 2. Light scattering from a dislocation in a single Si NW. (a) The schematic of a thin Si NW (left) and a dislocated Si NW (right, $\delta = 40$ nm) for TM polarization ($h = 50$ nm, $w = 100$ nm). The simulated surface electric charge density distribution ($\lambda = 800$ nm) is overlaid on the interface between two semi-infinite NWs (right), serving as a localized electric dipole p that radiates back into the guided modes of each semi-infinite NW. (b) and (c) The schematic of a dislocated Si NW with a larger height ($h = 180$ nm, $w = 100$ nm, $\delta = 40$ nm) for (b) TM and (c) TE polarizations. The simulated surface electric charge density distribution [(b), $\lambda = 800$ nm] and surface magnetic current density distribution [(c), $\lambda = 800$ nm] are overlaid on the interface between two semi-infinite NWs, serving as a localized electric quadrupole Q^e (b) (represented by a set of electric dipoles oriented anti-parallel in the horizontal and vertical directions, and a localized magnetic dipole m (c), respectively. In (a)–(c), the phases of the incident fields are chosen differently to clarify induced different multipolar sources of the scattered field.

incident light. As a result, the excitation for one handedness can be selectively enhanced through constructive interference, which occurs when these different excitation processes compensate for the $\pi/2$ phase shift between the TM- and TE-polarized components. Due to the anisotropic shape of NWs, this can simply be achieved by placing the optical resonances for these two polarizations at different spectral locations.

With all of the relevant design concepts in place, we are now in a position to use optical simulations to identify an optimal design for operation at the preselected wavelength of 800 nm, as schematically shown in Fig. 3(a). We start by considering a Si NW array without dislocations, i.e., with a displacement $\delta = 0$ nm, to optimize the direct transmission pathway for the light. Using the finite-element technique, we identify NW periods Λ_y, heights h, and widths w, for which the array serves as a half-wave plate, requiring a π phase shift between transmitted TM- and TE-polarized light. Whereas multiple geometries meet this basic requirement, we identify that a subwavelength period $\Lambda_y = 500$ nm offers easy-to-fabricate solutions and a high transmittance. Figure 3(b) shows the transmittance for different NW heights and widths together with a shaded region that highlights the set of solutions for which the phase shift between TM- and TE-polarized light is close to the desired value of π. Among these solutions, we choose the dimensions for the NWs as $h = 185$ nm and $w = 95$ nm [white dot in Fig. 3(b)], and we use these throughout this work for the Si NW arrays suspended in free space [Figs. 3(c), 3(d) and 4].

Next, we introduce a single dislocation in the NWs placed in an array and show how its geometrical properties can be designed to effectively couple both TM- and TE-polarized light to the same fundamental guided Bloch mode of the NW array [see Fig. 4(b) for the dispersion relation and the field distributions of the fundamental mode]. Figure 3(c) shows how the amplitudes and relative phase of the excited mode vary with the size of the dislocation for TM and TE polarizations (Supplement 1, Note 3). The amplitudes display a notable dependence on δ for both polarizations. Because each polarization induces distinct localized sources at the dislocation (Fig. 2), it is not surprising that the coupling cross sections for TM and TE polarizations vary differently with δ. This allows us to find a certain value of δ ($\neq 0$), where the amplitudes of the excited mode are identical for both polarizations. On the other hand, the relative phase of the excited waves is independent of δ and equal to $-\pi/2$ regardless of δ. This phase difference is strongly linked to the direct transmission properties of a Si NW array. From the coupled-mode theory, it follows that the phase difference must be $\pm\pi/2$ when a Si NW array serves as a half-wave plate in the direct transmission (Supplement 1, Note 4). In the scattered field description, this phase difference results from the relative phase of the total fields inside the semi-infinite NWs for the TM and TE polarizations. To produce a π phase shift in the direct transmission, the Si NW array operates near a Fabry–Perot resonance for TM polarization and off-resonance for TE polarization (Supplement 1, Fig. S4). This gives rise to the $\pi/2$ phase difference of the total fields inside the NWs for TM and TE polarizations, which is

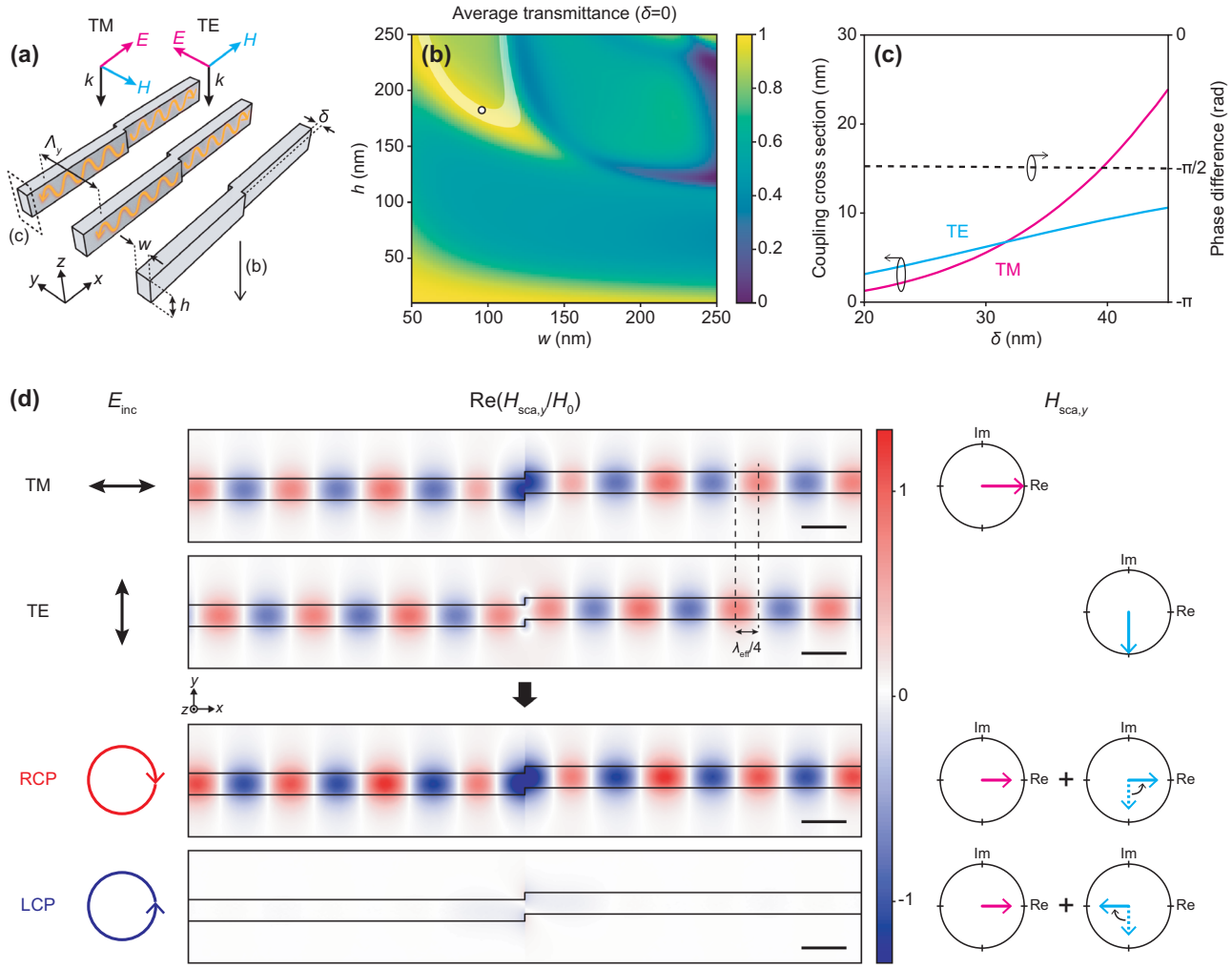

Fig. 3. Polarization-controlled excitation of guided waves at single dislocation. (a) The schematic of a single dislocation introduced into a Si NW array ($\Lambda_y = 500$ nm). For LPs, excited guided waves are examined at a position away from the dislocation (indicated by the black dashed box). (b) The simulated average transmittance ($\lambda = 800$ nm) of a non-dislocated Si NW array ($\delta = 0$) for LP illumination. The highlighted band indicates the set of the geometries, which provide the desired π phase shift (in a range of $\pm 0.05\pi$) between TM- and TE-polarized light in transmission. The white dot indicates the dimensions for the NWs used in (c) ($h = 185$ nm, $w = 95$ nm). (c) The simulated coupling cross sections (solid) and phase difference (dashed) of the fundamental guided mode ($\lambda = 800$ nm) excited for TM and TE polarizations as a function of δ ($\neq 0$). The coupling cross sections for LPs are identical around $\delta = 30$ nm. (d) The normalized scattered magnetic field distributions and their phasor representations ($\lambda = 800$ nm) for different incident polarizations. The phasor representations are broken down into contributions from TM- (magenta) and TE- (cyan) polarized incident fields to illustrate interference between them. Scale bar, 200 nm.

directly translated to the scattered fields by their induced sources at the dislocation.

Figure 3(d) shows the scattered field distributions of the single dislocation for different incident polarizations. From the scattered fields for TM and TE polarizations, we can see that the fundamental guided mode is launched from the dislocation and propagates along the semi-infinite Si NW array in both directions. As the dislocation size ($\delta = 30$ nm) is chosen to give rise to the same excitation amplitude for linear polarizations (LPs), the excited guided waves for TM and TE polarizations display the same magnitude but with a quarter effective wavelength delay between them dictated by the nanoscale geometry. When RCP (or LCP) is illuminated, both TM and TE polarization components contribute simultaneously to the excitation of the guided wave. Note that the incident CP provides additional $+\pi/2$ (or $-\pi/2$) phase delay between the excitation by the two LP components. Combined, the phase delay resulting from the nanostructure design and the CP excitation leads to constructive (or destructive) interference between the excited waves by TM and TE polarizations [Fig. 3(d)]. Therefore, only incident light for the RCP can excite the fundamental guided mode in the dislocated Si NW array. The phasor representation for the scattered fields is also shown for each incident polarization.

A single, subwavelength dislocation only couples a small fraction of the incident light at one very specific location. By periodically arranging dislocations in the Si NW array along the NW length, we can resonantly enhance the polarization-controlled excitation of the quasi-guided wave [Fig. 4(a)]. For an incident RCP plane wave, the fundamental mode is excited at each dislocation and quasi-guided waves are launched along the Si NW array [see Fig. 3(c)]. When the period Λ_x of the dislocations is chosen to be close to the effective wavelength of the fundamental mode, the quasi-guided waves excited at each dislocation interfere constructively with each other to build up a collective resonance

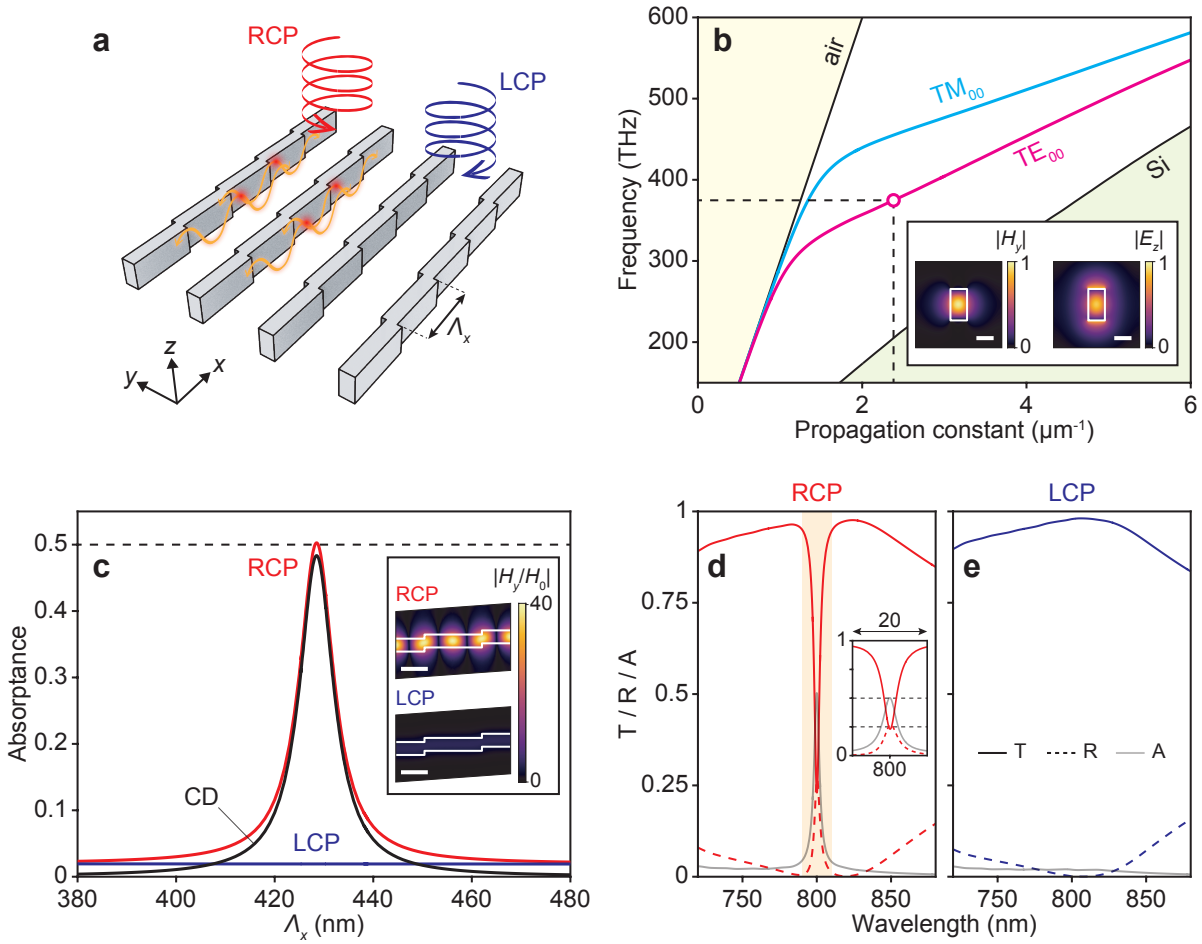

Fig. 4. Resonantly enhanced absorption using guided-mode resonance. (a) The schematic of periodic dislocations introduced into the Si NW array designed in Fig. 3. At each dislocation, the fundamental guided mode is excited for the RCP [Fig. 3(d)], and quasi-guided waves are launched along the Si NW array. (b) The simulated dispersion relations for the first two guided Bloch modes of the non-dislocated Si NW array. The white dot indicates the fundamental guided mode at $\lambda = 800$ nm. The black lines indicate the light lines in the air and the Si, respectively. Inset: Magnetic (left) and electric (right) field distributions of the guided mode at the point indicated in the dispersion relation. Scale bar, 100 nm. (c) The simulated absorptance ($\lambda = 800$ nm) for RCP (red) and LCP (blue) and corresponding CD (black) as a function of Λ_x. Inset: Normalized magnetic field distributions for the RCP (top) and the LCP (bottom) at the absorption peak ($\Lambda_x = 430$ nm). Scale bar, 200 nm. (d) and (e) Simulated transmittance (T, solid), reflectance (R, dashed), and absorptance (A, grey) spectra ($\Lambda_x = 430$ nm) for the RCP [red, (d)] and the LCP [blue, (e)]. Inset: Optical spectra for the RCP near the resonance wavelength (over the shaded range). The black dashed lines indicate 0.25 and 0.5, respectively.

(guided-mode resonance). The Q of such a resonance is limited by the material absorption and the amount of scattered light into free-space radiation at the dislocations. Given the weak material loss and small size of the dislocations, we can achieve a high-Q resonance [55–58]. The period needed to achieve a guided-mode resonance at the chosen operation wavelength of 800 nm can be approximately obtained from the simulated dispersion relation for the guided mode [Fig. 4(b)]. The resonance strongly enhances the RCP light absorption, while the incident light for LCP presents only weak, non-resonant absorption [Fig. 4(c)]. To maximize the resonant absorption from the guided-mode resonance, we can carefully adjust the radiative and absorption decay rates of the resonance to balance them. This is possible by exploring different combinations of NW heights and widths in the highlighted region in Fig. 3(b). For each combination of h and w, the other dimensions, δ and Λ_x, are determined accordingly as described above (Λ_y is fixed). This procedure enables us to achieve critical coupling for the dislocated Si NW array and a CD close to the theoretical limit of 0.5 (Supplement 1, Note 5). Note that the maximum value of the CD is slightly smaller than the theoretical limit due to the non-resonant absorption. This procedure led us to choose the NW dimensions above ($h = 185$ nm, $w = 95$ nm).

Figures 4(d) and 4(e) show the simulated transmission and reflection spectra of the periodically dislocated Si NW array for RCP and LCP, respectively. The spectra for the LCP display a high transmittance and low absorptance over a broad spectral range, with a slow overall variation that results from a spectrally broad Fabry–Perot resonance supported by the nanostructured film/NW array. On the other hand, the spectra for the RCP exhibit not only the broad Fabry–Perot resonance but also the spectrally narrow guided-mode resonance, which leads to strong resonant absorption. As these resonances are spectrally overlapped, the scattered light through the guided-mode resonance interferes with the transmitted light through the Fabry–Perot resonance, which gives rise to a large and spectrally narrow variation in both the transmission and reflection spectra for RCP. On the guided-mode resonance, both the total transmittance and reflectance become ~0.25 and allow us to achieve an absorptance of ~0.5.

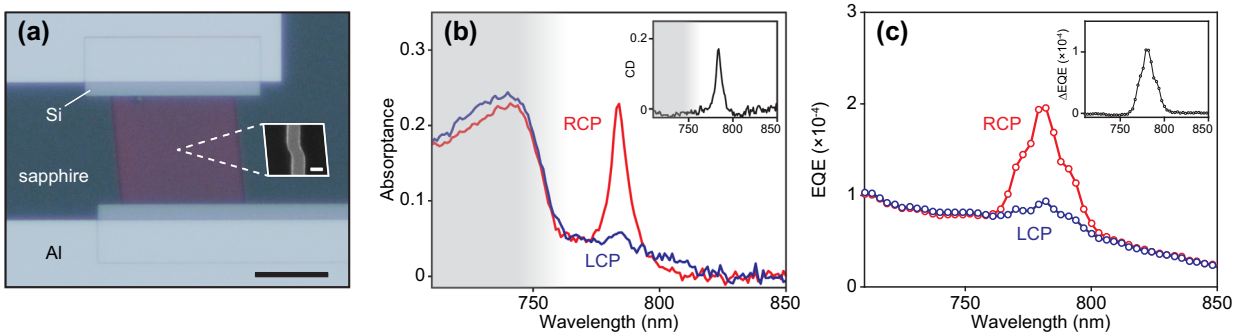

Fig. 5. Experimental demonstration of a CD photodetector. (a) The reflected optical micrograph of the fabricated CD photodetector under white-light illumination. Scale bar, 25 μm. Inset: SEM of a unit cell of the fabricated Si nanostructures. Scale bar, 50 nm. (b) The measured optical absorption spectra for the RCP (red) and the LCP (blue). Inset: Measured CD spectrum. The grayed-out areas in optical spectra indicate the spectral range in which first-order diffraction channels open up in the transparent substrate. (c) The measured EQE spectra for the RCP (red) and the LCP (blue). Inset: Measured differential EQE spectrum.

To experimentally demonstrate a CD photodetector, we fabricate a periodically dislocated Si NW array on a transparent sapphire substrate [Fig. 5(a)]. We slightly redesign the geometry of the dislocated Si NW array ($\Lambda_x = 370$ nm, $\Lambda_y = 430$ nm, $h = 320$ nm, $w = 65$ nm, and $\delta = 35$ nm) to take into account the presence of the substrate (Supplement 1, Fig. S6). For photocurrent extraction, we fabricate aluminum ohmic contacts at the ends of the dislocated Si NW array (43×37 μm^2). Next, we first characterize the optical absorption of the fabricated CD photodetector [Fig. 5(b)]. From transmission and reflection measurements, we calculate the absorptance by subtracting the transmittance and reflectance from unity. In the experimental absorption spectra, the dislocated Si NW array exhibits a high-Q optical resonance for the RCP light only. The sensitivity of the resonance to the handedness of the light results in a significant CD on resonance, corroborating the selective modal excitation described above. The grayed-out areas in the optical spectra correspond to the spectral range in which first-order diffraction channels open up in the transparent sapphire substrate. As the diffracted light is not captured in the measurements, the calculated absorptance is higher than the actual amount in this spectral range. With an applied external bias, we also characterize the photocurrent response of the CD photodetector [Fig. 5(c)]. For both RCP and LCP, the measured external quantum efficiency (EQE) spectra are consistent with the experimental optical absorption spectra. A resonantly enhanced EQE for RCP light over LCP light is observed, and we can use this to directly distinguish between these polarization states. Note that the spectral broadening of the EQE spectra, as compared to the absorption spectra, can be attributed to a spatially dependent charge collection efficiency (Supplement 1, Note 6). We also experimentally demonstrate a CD photodetector with resonant absorption and EQE for LCP by simply reversing the direction of the displacements for each of the dislocations (Supplement 1, Fig. S7).

3. CONCLUSION

In conclusion, we demonstrate the use of a nonlocal semiconductor metasurface to build an integrated photodetector for circularly polarized light. Using a dislocation as a building block, we are able to systematically design a Si metasurface that displays a guided-mode resonance only for a circular polarization of interest. The engineering of the resonance allows us to reach the theoretical maximum of CD in a symmetric external environment. We experimentally implement the metasurface in a CD photodetector and verify the key physics behind its operation using optical absorption and photocurrent measurements. These dislocated nanostructures can be employed in a range of applications for polarimetric sensing and imaging where dense integration is required.

Funding. Air Force Office of Scientific Research (FA9550-18-1-0323, FA9550-21-1-0312); U.S. Department of Energy (DE-FG07-ER46426); National Science Foundation (ECCS-2026822).

Acknowledgment. We would like to acknowledge support from an individual investigator from the Airforce, a Multidisciplinary University Research Initiative from the Air Force Office of Scientific Research, and from the Department of Energy. Part of this work was performed at the Stanford Nano Shared Facilities (SNSF) and the Stanford Nanofabrication Facility (SNF), supported by the National Science Foundation.

Disclosures. The authors declare no conflicts of interest.

Data availability. The data that support the plots within this paper and other findings of this study are available from the corresponding author upon reasonable request.

Supplemental document. See Supplement 1 for supporting content.

REFERENCES

1. Z. Bomzon, G. Biener, V. Kleiner, and E. Hasman, "Spatial Fourier-transform polarimetry using space-variant subwavelength metal-stripe polarizers," Opt. Lett. **26**, 1711–1713 (2001).
2. A. Pors, M. G. Nielsen, and S. I. Bozhevolnyi, "Plasmonic metagratings for simultaneous determination of Stokes parameters," Optica **2**, 716–723 (2015).
3. J. P. Balthasar Mueller, K. Leosson, and F. Capasso, "Ultracompact metasurface in-line polarimeter," Optica **3**, 42–47 (2016).
4. A. Basiri, X. Chen, J. Bai, P. Amrollahi, J. Carpenter, Z. Holman, C. Wang, and Y. Yao, "Nature-inspired chiral metasurfaces for circular polarization detection and full-Stokes polarimetric measurements," Light Sci. Appl. **8**, 78 (2019).
5. S. Yokogawa, S. P. Burgos, and H. A. Atwater, "Plasmonic color filters for CMOS image sensor applications," Nano Lett. **12**, 4349–4354 (2012).
6. M. L. Brongersma, "Plasmonic photodetectors, photovoltaics, and hot-electron devices," Proc. IEEE **104**, 2349–2361 (2016).
7. A. McClung, S. Samudrala, M. Torfeh, M. Mansouree, and A. Arbabi, "Snapshot spectral imaging with parallel metasystems," Sci. Adv. **6**, eabc7646 (2020).
8. M. I. Benetou, B. C. Thomsen, P. Bayvel, W. Dickson, and A. V. Zayats, "Four-level polarization discriminator based on a surface plasmon polaritonic crystal," Appl. Phys. Lett. **98**, 111109 (2011).

9. H. Park, Y. Dan, K. Seo, Y. J. Yu, P. K. Duane, M. Wober, and K. B. Crozier, "Filter-free image sensor pixels comprising silicon nanowires with selective color absorption," Nano Lett. **14**, 1804–1809 (2014).
10. Q. Li, J. van de Groep, Y. Wang, P. G. Kik, and M. L. Brongersma, "Transparent multispectral photodetectors mimicking the human visual system," Nat. Commun. **10**, 4982 (2019).
11. C. F. Bohren and D. R. Huffman, *Absorption and Scattering of Light by Small Particles* (Wiley, 1983).
12. L. Cao, J. S. White, J.-S. Park, J. A. Schuller, B. M. Clemens, and M. L. Brongersma, "Engineering light absorption in semiconductor nanowire devices," Nat. Mater. **8**, 643–647 (2009).
13. F. Afshinmanesh, J. S. White, W. Cai, and M. L. Brongersma, "Measurement of the polarization state of light using an integrated plasmonic polarimeter," Nanophotonics **1**, 125–129 (2012).
14. T.-H. Chiou, S. Kleinlogel, T. Cronin, R. Caldwell, B. Loeffler, A. Siddiqi, A. Goldizen, and J. Marshall, "Circular polarization vision in a stomatopod crustacean," Curr. Biol. **18**, 429–434 (2008).
15. J. F. Sherson, H. Krauter, R. K. Olsson, B. Julsgaard, K. Hammerer, I. Cirac, and E. S. Polzik, "Quantum teleportation between light and matter," Nature **443**, 557–560 (2006).
16. R. Farshchi, M. Ramsteiner, J. Herfort, A. Tahraoui, and H. T. Grahn, "Optical communication of spin information between light emitting diodes," Appl. Phys. Lett. **98**, 162508 (2011).
17. W. H. Brooks, W. C. Guida, and K. G. Daniel, "The significance of chirality in drug design and development HHS public access," Curr. Top. Med. Chem. **11**, 760–770 (2011).
18. D. A. Talmage and P. J. Curran, "Remote sensing using partially polarized light," Int. J. Remote Sens. **7**, 47–64 (1986).
19. E. Maguid, I. Yulevich, D. Veksler, V. Kleiner, M. L. Brongersma, and E. Hasman, "Photonic spin-controlled multifunctional shared-aperture antenna array," Science **352**, 1202–1206 (2016).
20. N. A. Rubin, G. D'Aversa, P. Chevalier, Z. Shi, W. T. Chen, and F. Capasso, "Matrix Fourier optics enables a compact full-Stokes polarization camera," Science **365**, eaax1839 (2019).
21. J. R. Schaibley, H. Yu, G. Clark, P. Rivera, J. S. Ross, K. L. Seyler, W. Yao, and X. Xu, "Valleytronics in 2D materials," Nat. Rev. Mater. **1**, 16055 (2016).
22. L. Lu, J. D. Joannopoulos, and M. Soljačić, "Topological photonics," Nat. Photonics **8**, 821–829 (2014).
23. Y. Yang, R. C. da Costa, M. J. Fuchter, and A. J. Campbell, "Circularly polarized light detection by a chiral organic semiconductor transistor," Nat. Photonics **7**, 634–638 (2013).
24. C. Chen, L. Gao, W. Gao, C. Ge, X. Du, Z. Li, Y. Yang, G. Niu, and J. Tang, "Circularly polarized light detection using chiral hybrid perovskite," Nat. Commun. **10**, 1927 (2019).
25. A. Ishii and T. Miyasaka, "Direct detection of circular polarized light in helical 1D perovskite-based photodiode," Sci. Adv. **6**, eabd3274 (2020).
26. W. Li, Z. J. Coppens, L. V. Besteiro, W. Wang, A. O. Govorov, and J. Valentine, "Circularly polarized light detection with hot electrons in chiral plasmonic metamaterials," Nat. Commun. **6**, 8379 (2015).
27. M. Hentschel, M. Schäferling, X. Duan, H. Giessen, and N. Liu, "Chiral plasmonics," Sci. Adv. **3**, 1–13 (2017).
28. J. K. Gansel, M. Thiel, M. S. Rill, M. Decker, K. Bade, V. Saile, G. Von Freymann, S. Linden, and M. Wegener, "Gold helix photonic metamaterial as broadband circular polarizer," Science **325**, 1513–1515 (2009).
29. Y. Zhao, M. A. Belkin, and A. Alù, "Twisted optical metamaterials for planarized ultrathin broadband circular polarizers," Nat. Commun. **3**, 870 (2012).
30. J. Lin, J. P. B. Mueller, Q. Wang, G. Yuan, N. Antoniou, X.-C. Yuan, and F. Capasso, "Polarization-controlled tunable directional coupling of surface plasmon polaritons," Science **340**, 331–334 (2013).
31. H. Kwon, D. Sounas, A. Cordaro, A. Polman, and A. Alù, "Nonlocal metasurfaces for optical signal processing," Phys. Rev. Lett. **121**, 173004 (2018).
32. F. Yesilkoy, E. R. Arvelo, Y. Jahani, M. Liu, A. Tittl, V. Cevher, Y. Kivshar, and H. Altug, "Ultrasensitive hyperspectral imaging and biodetection enabled by dielectric metasurfaces," Nat. Photonics **13**, 390–396 (2019).
33. C. Guo, H. Wang, and S. Fan, "Squeeze free space with nonlocal flat optics," Optica **7**, 1133–1138 (2020).
34. A. C. Overvig, S. C. Malek, and N. Yu, "Multifunctional nonlocal metasurfaces," Phys. Rev. Lett. **125**, 017402 (2020).
35. M. Lawrence, D. R. Barton, III, J. Dixon, J.-H. Song, J. van de Groep, M. L. Brongersma, and J. A. Dionne, "High quality factor phase gradient metasurfaces," Nat. Nanotechnol. **15**, 956–961 (2020).
36. S. J. Kim and M. L. Brongersma, "Active flat optics using a guided mode resonance," Opt. Lett. **42**, 5–8 (2017).
37. S. C. Malek, A. C. Overvig, S. Shrestha, and N. Yu, "Active nonlocal metasurfaces," Nanophotonics **10**, 655–665 (2020).
38. H. A. Haus, *Waves and Fields in Optoelectronics* (Prentice-Hall, 1984).
39. S. Fan, W. Suh, and J. D. Joannopoulos, "Temporal coupled-mode theory for the Fano resonance in optical resonators," J. Opt. Soc. Am. A **20**, 569–572 (2003).
40. W. Woltersdorff, "Über die optischen Konstanten dünner Metallschichten im langwelligen Ultrarot," Zeitschrift für Phys. **91**, 230–252 (1934).
41. X. Yin, T. Steinle, L. Huang, T. Taubner, M. Wuttig, T. Zentgraf, and H. Giessen, "Beam switching and bifocal zoom lensing using active plasmonic metasurfaces," Light Sci. Appl. **6**, e17016 (2017).
42. X. Yin, M. Schäferling, B. Metzger, and H. Giessen, "Interpreting chiral nanophotonic spectra: the plasmonic Born-Kuhn model," Nano Lett. **13**, 6238–6243 (2013).
43. A. Papakostas, A. Potts, D. M. Bagnall, S. L. Prosvirnin, H. J. Coles, and N. I. Zheludev, "Optical manifestations of planar chirality," Phys. Rev. Lett. **90**, 107404 (2003).
44. V. K. Valev, J. J. Baumberg, C. Sibilia, and T. Verbiest, "Chirality and chiroptical effects in plasmonic nanostructures: fundamentals, recent progress, and outlook," Adv. Mater. **25**, 2517–2534 (2013).
45. D. Lin, P. Fan, E. Hasman, and M. L. Brongersma, "Dielectric gradient metasurface optical elements," Science **345**, 298–302 (2014).
46. S. Yi, M. Zhou, Z. Yu, P. Fan, N. Behdad, D. Lin, K. X. Wang, S. Fan, and M. Brongersma, "Subwavelength angle-sensing photodetectors inspired by directional hearing in small animals," Nat. Nanotechnol. **13**, 1143–1147 (2018).
47. G. I. Taylor, "The mechanism of plastic deformation of crystals. Part I.—Theoretical," Proc. R. Soc. London. Ser. A **145**, 362–387 (1934).
48. M. Raukas, and S. Gorsky, R. Zhang, A. Gok, R. Wang, K. Kebede, A. Lenef, and L. D. Negro, "Directional light emission enhancement from LED-phosphor converters using dielectric Vogel spiral arrays," APL Photon. **126103**, 126103 (2019).
49. A. S. Meeussen, E. C. Oğuz, Y. Shokef, and M. van Hecke, "Topological defects produce exotic mechanics in complex metamaterials," Nat. Phys. **16**, 307–311 (2020).
50. M. Baraclough, I. R. Hooper, and W. L. Barnes, "Direct observation of defect modes in molecular aggregate analogs," Phys. Rev. B **102**, 224105 (2020).
51. V. C. Nguyen, L. Chen, and K. Halterman, "Total transmission and total reflection by zero index metamaterials with defects," Phys. Rev. Lett. **105**, 233908 (2010).
52. E. Maguid, M. Yannai, A. Faerman, I. Yulevich, V. Kleiner, and E. Hasman, "Disorder-induced optical transition from spin Hall to random Rashba effect," Science **358**, 1411–1415 (2017).
53. M. Yannai, E. Maguid, A. Faerman, Q. Li, J. H. Song, V. Kleiner, M. L. Brongersma, and E. Hasman, "Order and disorder embedded in a spectrally interleaved metasurface," ACS Photon. **5**, 4764–4768 (2018).
54. A. I. Kuznetsov, A. E. Miroshnichenko, M. L. Brongersma, Y. S. Kivshar, and B. Luk'yanchuk, "Optically resonant dielectric nanostructures," Science **354**, 2472 (2016).
55. G. Quaranta, G. Basset, O. J. F. Martin, and B. Gallinet, "Recent advances in resonant waveguide gratings," Laser Photon. Rev. **12**, 1800017 (2018).
56. R. Magnusson and S. S. Wang, "New principle for optical filters," Appl. Phys. Lett. **61**, 1022 (1992).
57. H. Liu and P. Lalanne, "Microscopic theory of the extraordinary optical transmission," Nature **452**, 728–731 (2008).
58. U. Fano, "The theory of anomalous diffraction gratings and of quasi-stationary waves on metallic surfaces (Sommerfeld's Waves)," J. Opt. Soc. Am. **31**, 213–222 (1941).